

Second Harmonic Generation and Hyperpolarizabilities of the Double-Cubane Compound $[\text{Sb}_7\text{S}_8\text{Br}_2](\text{AlCl}_4)_3$: Chalcogenide in Ionic Liquids

Ali Hussain Reshak,^{*,†,‡} H. Kamarudin,[‡] S. Auluck,[§] and I.V. Kityk^{||}

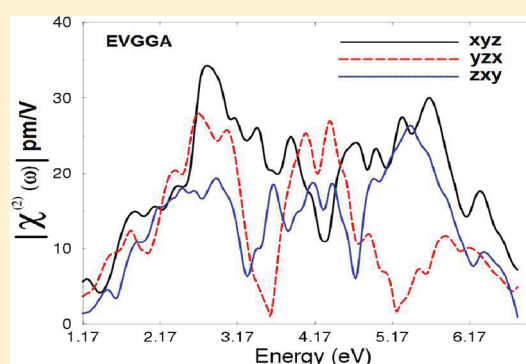
[†]Institute of Physical Biology, South Bohemia University, Nove Hradky 37333, Czech Republic

[‡]School of Material Engineering, Malaysia University of Perlis, P. O. Box 77, d/a Pejabat Pos Besar, 01007 Kangar, Perlis, Malaysia

[§]National Physical Laboratory Dr. K S Krishnan Marg, New Delhi 110012, India

^{||}Electrical engineering Department, Technological University of Czestochowa, Aleja Armii Krajowej 17/19, Czestochowa, Poland

ABSTRACT: Because noncentrosymmetric $[\text{Sb}_7\text{S}_8\text{Br}_2](\text{AlCl}_4)_3$ single crystals possess a wide optical transparency region, it is a promising material for nonlinear optical applications. We have calculated the dispersion of linear and nonlinear optical susceptibilities including optical second harmonic generation (SHG) using a relaxed geometry. We find that the fundamental optical absorption edge situated at about 2.03 eV is in excellent agreement with the experimental data. Calculations of $\epsilon_2^{xx}(\omega)$, $\epsilon_2^{yy}(\omega)$, and $\epsilon_2^{zz}(\omega)$ tensor components of the frequency-dependent dielectric function are presented. The single crystal possesses a considerable anisotropy of linear optical susceptibilities, which usually favors an enhanced phase matching conditions necessary to observe SHG and optical parametric oscillator (OPO) effects. Our calculations show that, in $[\text{Sb}_7\text{S}_8\text{Br}_2](\text{AlCl}_4)_3$, $|\chi_{123}^{(2)}(\omega)|$ is the principal tensor component having the highest value of SHG at zero frequency limit as well as at 1.165 eV ($\lambda = 1064$ nm) laser wavelength generation. The microscopic second-order hyperpolarizability, β_{123} , of the dominant SHG component is calculated at the static limit and at $\lambda = 1064$ nm.



I. INTRODUCTION

An ionic liquid (IL) is a salt in the liquid-state phase. Sometimes the term has been limited to description of salts whose melting point is below some arbitrary temperature, such as 100 °C (212 °F). While ordinary liquids such as water and gasoline are prevalently built from electrically neutral molecules, ionic liquids are largely constructed from ions and short-lived ion pairs. These substances are also called liquid electrolytes, ionic melts, ionic fluids, fused salts, liquid salts, or ionic glasses. Ionic liquids have many applications, such as powerful solvents and electrically conducting fluids (electrolytes). Salts that are liquid at near-ambient temperature are crucial for modern electric battery applications and have been used as sealants due to their very low vapor pressure. Any salt that melts without decomposing or vaporizing usually yields an IL. Sodium chloride (NaCl), for example, melts at 801 °C (1474 °F) into a liquid phase consisting mainly largely of sodium cations (Na^+) and chloride anions (Cl^-). Conversely, when an IL is cooled, it often forms an ionic solid which may be either crystalline-like or glassy. The ionic bond is usually stronger than the weak van der Waals forces between the molecules of ordinary liquids. For that reason, common salts favor melting at higher temperatures than other solid molecules. Some salts are liquid at or below room temperature. Examples may include pyridinium chloride, $\text{C}_5\text{H}_6\text{N}^+ \cdot \text{Cl}^-$, which melts at 144.5 °C (292.1 °F);¹ 1-ethyl-3-methylimidazolium dicyanamide, $(\text{C}_2\text{H}_5)(\text{CH}_3)_2\text{C}_3\text{H}_3\text{N}_2^+ \cdot \text{N}(\text{CN})_2^-$, which melts at

−21 °C (−6 °F);² and 1-butyl-3,5-dimethylpyridinium bromide, which becomes a glass below −24 °C (−11 °F).³ Low-temperature ionic liquid can be compared to ionic solutions. Certain mixtures of nitrate salts can give melting points below 100 °C.⁴ The term “ionic liquid” in the general sense was used as early as 1943.⁵

Ionic liquids as supersolvents are now recognized as powerful reaction media for preparing functional materials such as zeolites,⁶ metal–organic frameworks,⁶ metal nanoparticles,⁷ and organic compounds,⁸ as well as being useful in separations,⁹ electrochemistry,¹⁰ and nanotechnology.¹¹ Their biggest use is in the production of laundry detergents. They are also used in medicine and in agriculture, helping to improve human life. Chalcogenides have not only diverse structures but also technologically promising properties such as thermoelectricity and solar energy conversion;¹² phase change transitions liquids could offer fascinating opportunities for fabrication of new structure in chalcogenides and unprecedented properties.¹³ Recently Zhang et al.¹³ demonstrated the use of the ionic liquid (EMIM)Br– AlCl_3 (EMIM = 1-ethyl-3-methylimidazolium) as solvent for fabrication of a new material featuring a cationic chalcogenide. They report for the first time the synthesis of cationic chalcogenide

Received: April 24, 2011

Revised: August 30, 2011

Published: September 07, 2011

clusters in ionic liquids and show that chalcogenide polycationic clusters can be conveniently synthesized in ionic liquid media containing Lewis acids or strong acceptors. They have found that the red crystals of $[\text{Sb}_7\text{S}_8\text{Br}_2](\text{AlCl}_4)_3$ exhibit nonlinear optical (NLO) properties, including difference-frequency generation (DFG) and second harmonic generation (SHG). Since the $[\text{Sb}_7\text{S}_8\text{Br}_2](\text{AlCl}_4)_3$ single crystals possess a wide optical transparency region and are noncentrosymmetric, it is interesting to calculate the linear and nonlinear optical susceptibilities in order to understand the functionality of these materials and how it does work to find more application in our daily life. In this paper we present results of such calculations based on density functional theory.

Section II describes the structural aspects, and section III is devoted to describing the basic theoretical aspects. Section IV is devoted to verification of our results pertaining to the linear and nonlinear optical susceptibilities of the double-cubane compound $[\text{Sb}_7\text{S}_8\text{Br}_2](\text{AlCl}_4)_3$. The summary and principal conclusions are given in section V.

II. STRUCTURAL ASPECTS

Recently Zhang et al.¹³ synthesized the double-cubane compound $[\text{Sb}_7\text{S}_8\text{Br}_2](\text{AlCl}_4)_3$ for the first time, by reacting Sb with S in (EMIM)Br– AlCl_3 ionic liquid (1:11 (EMIM)Br/ AlCl_3 molar ration) at 165 °C for 10 days. The structure was determined from single-crystal X-ray diffraction data collected at 100 K on a STOE 2T imaging-plate diffraction system with graphite-monochromatized Mo K α radiation. A numerical and empirical absorption correction was applied; direct methods and full-matrix least-squares refinements against F^2 were performed with the SHELXTL computer package program.¹³ $[\text{Sb}_7\text{S}_8\text{Br}_2](\text{AlCl}_4)_3$ crystallizes in the noncentrosymmetric orthorhombic space group $P2_12_12_1$, with $Z = 4$, $a = 11.989(2)$ Å, $b = 16.896(3)$ Å, $c = 17.378(4)$ Å, and $v = 3520.2(12)$ Å³. Other parameters of the data are $T = 100$ K, $2\theta_{\text{max}}(\text{Mo K}\alpha) = 53.52^\circ$, and $D_{\text{calc}} = 3.349$ g/cm³.¹³ The crystal structure of $[\text{Sb}_7\text{S}_8\text{Br}_2](\text{AlCl}_4)_3$ consists of cationic $[\text{Sb}_7\text{S}_8\text{Br}_2]^{3+}$ clusters and $[\text{AlCl}_4]^-$ anions. Each cluster adopts a unique double-cubane structure in which two distorted cubic clusters are connected by sharing one corner-Sb1 site. The other corners are alternately occupied with Sb and S atoms. Two Sb sites Sb2 and Sb6 have terminal Sb–Br bonds projecting out of the cluster structure; for more details see ref 13.

Our previous calculations¹⁴ show that $[\text{Sb}_7\text{S}_8\text{Br}_2](\text{AlCl}_4)_3$ possesses a wide energy band gap. The upper valence band has a maximum at the S point of the Brillouin zone, while the conduction band minimum is located at the Y point resulting in an indirect energy band gap. Also we have evaluated¹⁴ the electronic charge space density contour in four planes, namely, (001), (110), (100), and (010), which show that this compound possesses a considerable anisotropy. Generally a crystal which shows considerable anisotropy favors enhanced phase matching conditions necessary for the SHG and optical parametric oscillator (OPO).¹⁵

III. THEORETICAL CALCULATION

We have optimized the atomic positions of the atoms in $[\text{Sb}_7\text{S}_8\text{Br}_2](\text{AlCl}_4)_3$, starting from the positions taken from the X-ray diffraction data,¹³ by minimization of the forces acting on the atoms, keeping the lattice parameters fixed at the experimental values. We have used the optimized structure as input parameters for the present calculations of the linear and

nonlinear optical susceptibilities. Once the forces are minimized in this construction, one can then find the self-consistent density at these positions by turning off the relaxations and driving the system to self-consistency. The linear and nonlinear optical susceptibilities and various spectroscopic features can be determined from the relaxed geometry.

The all-electron full potential linearized augmented plane wave (FP-LAPW) method based on the density functional theory (DFT)¹⁶ as implemented in WIEN2K code¹⁷ was used to perform the present calculations. The Ceperley–Alder (CA) local density approximation (LDA),¹⁸ which is based on exchange-correlation energy optimization to calculate the total energy, was employed. The well-known LDA underestimation of the band gaps may give incorrect linear and nonlinear optical susceptibilities, especially the nonlinear optical susceptibilities, since they are more sensitive to the band gaps than the linear optical susceptibilities due to higher power energy differences in the denominators of the nonlinear optical susceptibilities formalism. Also in the static limit, the nonlinear optical susceptibilities show the general trend of having an inverse correlation with the band energy gap. To avoid this problem, we have used in addition the Engel–Vosko generalized gradient approximation (EV-GGA),¹⁹ which optimizes the corresponding potential for linear and nonlinear optical susceptibilities calculations.

The muffin-tin radii were assumed to be 2.29 atomic units (au) for Sb and S, 2.32 au for Br, and 1.97 au for Al and Cl. The wave functions in the interstitial regions were expanded in a plane waves basis set with a cutoff energy up to $K_{\text{max}} = 9/R_{\text{MT}}$, to achieve energy eigenvalues convergence, where R_{MT} denotes the smallest atomic sphere radius and K_{max} gives the magnitude of the largest K vector in the plane wave expansion. The valence wave functions inside the spheres were expanded up to $l_{\text{max}} = 10$ while the charge density was Fourier expanded up to $G_{\text{max}} = 12$ (au)^{−1}. Self-consistency was achieved by use of 300 k -points in the irreducible Brillouin zone (IBZ). The linear and nonlinear optical susceptibilities were calculated using 1000 k -points in the IBZ. Both the muffin-tin radius and the number of k -points were varied to ensure total energy convergence. The self-consistent calculations are converged since the total energy of the system is stable within 10^{-5} Ry.

IV. RESULTS AND DISCUSSION

The double-cubane compound was synthesized in the form of a single crystal and crystallizes in the noncentrosymmetric orthorhombic space group $P2_12_12_1$. This symmetry allows three nonzero components of the second-order dielectric (optical) tensor corresponding to the electric field E being directed along a , b , and c crystallographic axes. The single crystal possesses well-pronounced structures of the three principal complex tensor components $\epsilon^{xx}(\omega)$, $\epsilon^{yy}(\omega)$, and $\epsilon^{zz}(\omega)$. The imaginary part of the three principal complex tensor components completely defines the linear optical susceptibilities. The imaginary part of the three principal complex tensor components originates from interband transitions between valence and conduction band states. According to the dipolar selection rule only transitions changing the angular momentum quantum number l by unity ($\Delta = \pm 1$) are allowed. The electronic band structure of this single crystal suggests that the first spectral peak in $\epsilon_2^{xx}(\omega)$, $\epsilon_2^{yy}(\omega)$, and $\epsilon_2^{zz}(\omega)$ is due to the transition from Sb-s/d, S-p, Cl-p, and Br-p to Sb-p, Cl-s/p, and S-p states, while the second peak corresponds to the Sb-p/d, S-p, Al-p, and Cl-p to Sb-p/d, S-p, Br-d, and S-s transition.

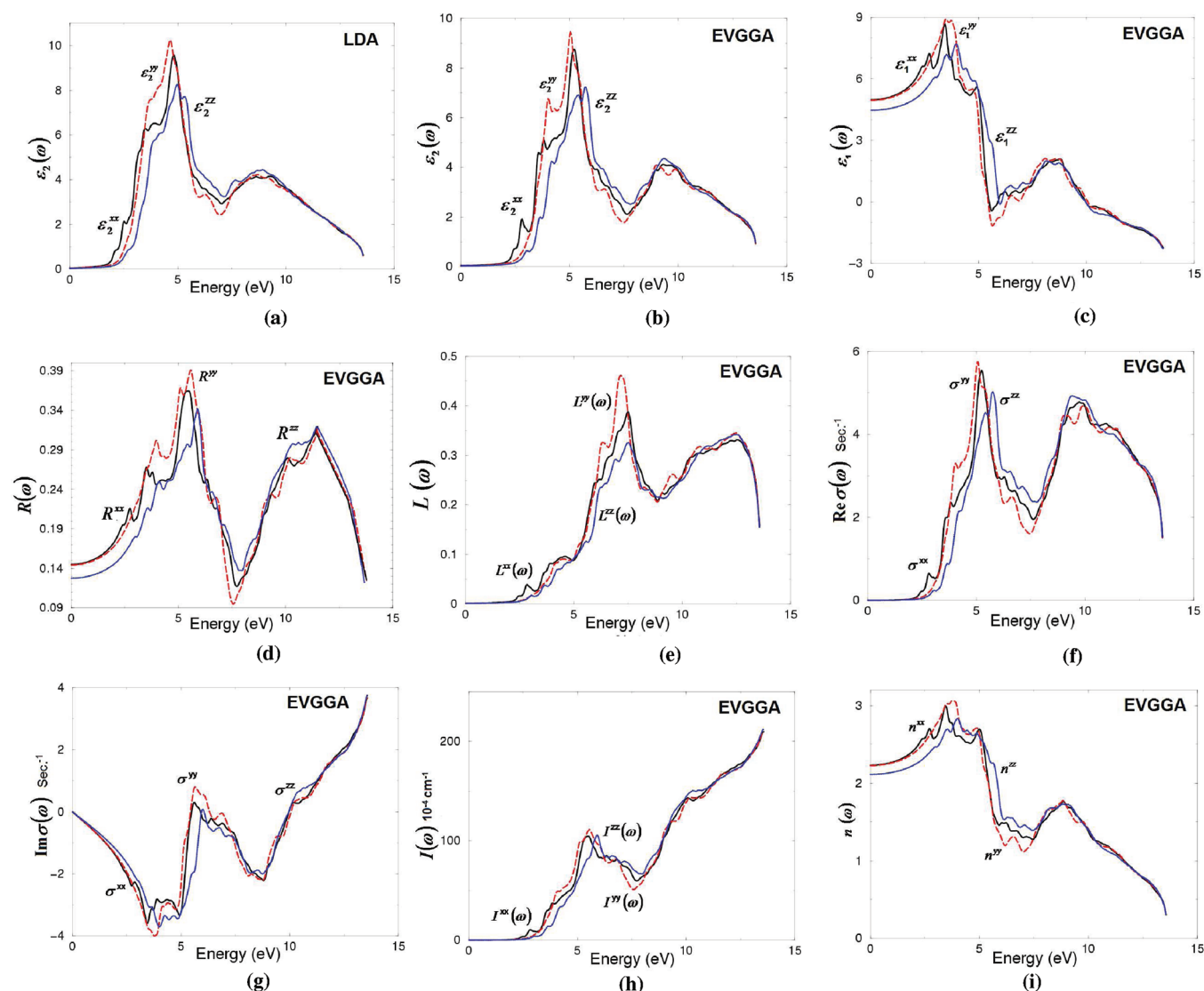


Figure 1. Calculated $\epsilon_2^{xx}(\omega)$ (dark solid curve, black color online), $\epsilon_2^{yy}(\omega)$ (light dashed curve, red color online), and $\epsilon_2^{zz}(\omega)$ (light solid curve, blue color online) dispersion spectra: (a) LDA; (b) EVGGA with scissors correction. (c) Calculated $\epsilon_1^{xx}(\omega)$ (dark solid curve, black color online), $\epsilon_1^{yy}(\omega)$ (light dashed curve, red color online), and $\epsilon_1^{zz}(\omega)$ (light solid curve, blue color online) spectra using EVGGA with scissors correction. (d) Calculated $R^{xx}(\omega)$ (dark solid curve, black color online), $R^{yy}(\omega)$ (light dashed curve, red color online), and $R^{zz}(\omega)$ (light solid curve, blue color online) using EVGGA with scissors correction. (e) Calculated loss function $L^{xx}(\omega)$ (dark solid curve, black color online), $L^{yy}(\omega)$ (light dashed curve, red color online), and $L^{zz}(\omega)$ (light solid curve, blue color online) spectrum using EVGGA with scissors correction. (f) Calculated real part of the conductivity of $\sigma^{xx}(\omega)$ (dark solid curve, black color online), $\sigma^{yy}(\omega)$ (light dashed curve, red color online), and $\sigma^{zz}(\omega)$ (light solid curve, blue color online) spectrum using EVGGA with scissors correction, the optical conductivity in 10^{15} s^{-1} . (g) Calculated imaginary part of the conductivity of $\sigma^{xx}(\omega)$ (dark solid curve, black color online), $\sigma^{yy}(\omega)$ (light dashed curve, red color online), and $\sigma^{zz}(\omega)$ (light solid curve, blue color online) spectrum using EVGGA with scissors correction, the optical conductivity in 10^{15} s^{-1} . (h) Calculated absorption coefficient $I^{xx}(\omega)$ (dark solid curve, black color online), $I^{yy}(\omega)$ (light dashed curve, red color online), and $I^{zz}(\omega)$ (light solid curve, blue color online) spectrum using EVGGA with scissors correction, the absorption coefficient in 10^4 s^{-1} . (i) Calculated refractive indices $n^{xx}(\omega)$ (dark solid curve, black color online), $n^{yy}(\omega)$ (light dashed curve, red color online), and $n^{zz}(\omega)$ (light solid curve, blue color online) spectrum using EVGGA with scissors correction.

A remarkable fact regarding the first peak in $\epsilon_2^{xx}(\omega)$, $\epsilon_2^{yy}(\omega)$, and $\epsilon_2^{zz}(\omega)$ is that its width is essentially determined by the width of the highest occupied valence band.

The fundamental optical absorption edge for $\epsilon_2^{xx}(\omega)$, $\epsilon_2^{yy}(\omega)$, and $\epsilon_2^{zz}(\omega)$, located at 1.6 eV (2.03 eV) using LDA (EV-GGA), are presented in Figure 1a,b. The difference between LDA and EV-GGA is attributed to the fact that LDA underestimates the band gaps and EV-GGA may correct this underestimate. LDA is based on simple model assumptions which are not sufficiently flexible to reproduce accurately the exchange correlation energy

and its charge space derivative. While the EV-GGA approach is able to reproduce better exchange potential at the expense of less agreement in the exchange energy and yields better band splitting compared to LDA.

The dispersion of the imaginary part of these complex components presents two main spectral features. The first one is located between 2.0 and 7.5 eV and shows considerable anisotropy between the three principal complex tensor components. The second structure, located between 7.5 and 13.5 eV, shows considerable anisotropy up to 10.0 eV (see Figure 1a,b).

Table 1. Calculated $\epsilon_1^{xx}(0)$, $\epsilon_1^{yy}(0)$, $\epsilon_1^{zz}(0)$, $n^{xx}(\omega)$, $n^{yy}(\omega)$, $n^{zz}(\omega)$, and $\Delta n(\omega)$

	theoretical
$\epsilon_1^{xx}(\omega)$	$\epsilon_1^{xx}(0) = 4.97$ $\epsilon_1^{xx}(\omega)$ (at 1064 nm) = 5.21
$\epsilon_1^{yy}(\omega)$	$\epsilon_1^{yy}(0) = 4.95$ $\epsilon_1^{yy}(\omega)$ (at 1064 nm) = 5.16
$\epsilon_1^{zz}(\omega)$	$\epsilon_1^{zz}(0) = 4.45$ $\epsilon_1^{zz}(\omega)$ (at 1064 nm) = 4.61
$n^{xx}(\omega)$	$n^{xx}(0) = 2.23$ $n^{xx}(\omega)$ (at 1064 nm) = 2.29
$n^{yy}(\omega)$	$n^{yy}(0) = 2.22$ $n^{yy}(\omega)$ (at 1064 nm) = 2.28
$n^{zz}(\omega)$	$n^{zz}(0) = 2.11$ $n^{zz}(\omega)$ (at 1064 nm) = 2.15
$\Delta n(\omega)$	$\Delta n(0) = 0.115$ $\Delta n(\omega)$ (at 1064 nm) = 0.135

We should emphasize that this anisotropy in the linear optical susceptibilities favors enhanced phase matching conditions necessary for observation of the SHG and OPO.

Following Figure 1a,b, one can emphasize that the EVGGA approach has significant effect on the spectral structures of the three components: $\epsilon_2^{xx}(\omega)$, $\epsilon_2^{yy}(\omega)$, and $\epsilon_2^{zz}(\omega)$ as all the structures are spectrally shifted toward higher energies by around 0.4 eV. Scissors correction can bring the calculated energy band gap closer to the experimental (2.03 eV¹³). For EV-GGA we need a smaller scissors correction compared to LDA.

The real parts $\epsilon_1^{xx}(\omega)$, $\epsilon_1^{yy}(\omega)$, and $\epsilon_1^{zz}(\omega)$ of the corresponding principal complex tensor components, obtained from the imaginary part by means of Kramers–Kronig transformation,²⁰ are shown in Figure 1c. The calculated static dielectric constants $\epsilon_1^{xx}(0)$, $\epsilon_1^{yy}(0)$, and $\epsilon_1^{zz}(0)$ are presented in Table 1. With the aid of the existing information about the calculated imaginary and real parts of the principal complex tensor components one can evaluate other optical properties such as reflectivity spectra $R(\omega)$, refractive indices $n(\omega)$, birefringence $\Delta n(\omega)$, absorption coefficient $I(\omega)$, conductivity $\sigma(\omega)$, and loss function $L(\omega)$.

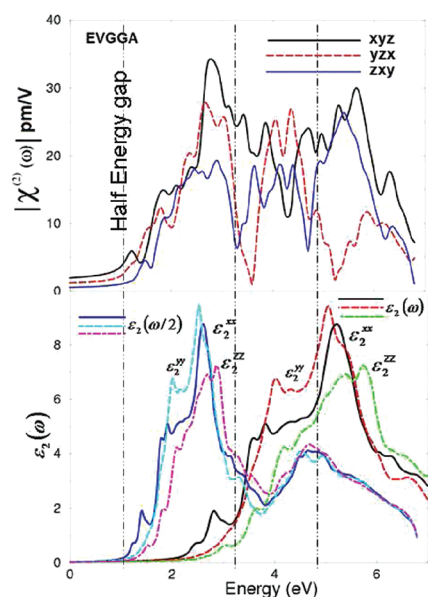
The reflectivity spectra along x -, y -, and z -axes are depicted in Figure 1d. From the obtained reflectivity spectra, we can note that at low energies 0–6.0 eV, the optical reflectivity starts at about 0.15% for x - and y -components and at 0.13% for the z -component; thereafter, x -, y -, and z -components increase to about 37, 39, and 34%, respectively, forming a strong reflectivity maximum. The second strong reflectivity maximum occurs at higher energies around 12.0 eV. The three components increase up to about 32%. Important transitions are from s -states of valence bond (VB) to p -states of covalence bond (CB). The reflectivity spectrum reproduces the positions of the peaks determined by interband transitions with good accuracy. It is interesting that there is an abrupt reduction in the reflectivity spectrum at energy of about 12.5 eV, confirming the occurrence of a collective plasmon resonance. The depth of the plasmon minimum is determined by the imaginary part of the dielectric function at the plasma resonance and is representative of the degree of overlap between the interband absorption regions.

The calculated energy-loss function $-\text{Im}(\epsilon^{-1}(\omega))$ is presented in Figure 1e. The function $-\text{Im}(\epsilon^{-1}(\omega))$ describes the energy loss of the fast electron, traversing the material. The sharp

maxima in the energy-loss function is associated with the existence of plasma oscillations. The plasmon losses correspond to a collective oscillation of the valence electrons, and their energies are related to the density of valence electrons. In the case of interband transitions, which consist prevalently from plasmon excitations, the scattering probability for volume losses is directly connected to the energy-loss function. There are other features in this spectrum, in addition to the plasmon peak, associated with interband transitions. The plasmon peak is usually the most intense feature in the spectrum, and this is at energy where $\epsilon_1(\omega)$ crosses zero. The energy of the maximum peak of $-\text{Im}(\epsilon^{-1}(\omega))$ for $L^{xx}(\omega)$, $L^{yy}(\omega)$, and $L^{zz}(\omega)$ of this single crystal is assigned to the energy of volume plasmon $\hbar\omega_p$. The plasma frequency $\hbar\omega_p$ can be calculated by means of energy-loss function $-\text{Im}(\epsilon^{-1}(\omega))$ and can be tested with f -sum rule,²¹ $\pi/2\omega_p^2 = \int_0^\infty \text{Im}(\epsilon(\omega))\omega d\omega$. The optical conductivity can be calculated from the principal complex tensor components. Following Figure 1f,g, one can see that the real part of the optical conductivity presents the general features of the imaginary part of the principal complex tensor components, while reducing the amplitude of the first structure (2.03–7.5 eV) and increasing the amplitude of the second structure (7.5–13.5 eV). The imaginary part of the optical conductivity shows the reverse features of the real part of the principal complex tensor components with spectral shifting the optical conductivity to be zero. The absorption coefficient of $[\text{Sb}_7\text{S}_8\text{Br}_2](\text{AlCl}_4)_3$, as presented at Figure 1h, shows the fundamental optical absorption edge located at 2.03 eV ($\lambda = 611$ nm) using EV-GGA in excellent agreement with the experimental data.¹³ This fact supports our previous observation of the fundamental optical absorption edge for $\epsilon_2^{xx}(\omega)$, $\epsilon_2^{yy}(\omega)$, and $\epsilon_2^{zz}(\omega)$ (Figure 1a,b). After the fundamental optical absorption edge the absorption coefficient increases drastically and forms the first absorption peak situated around 6.0 eV. Then the absorption coefficient is reduced to the first valley at 7.5 eV and again is enhanced rapidly to reach its maximum value at around 13.5 eV ($\lambda = 92.0$ nm). It is necessary to emphasize that the single crystal $[\text{Sb}_7\text{S}_8\text{Br}_2](\text{AlCl}_4)_3$ possesses a wide optical transparency region (3.57–7.81 μm).

The calculated refractive index dispersions are shown in Figure 1i. The calculated values of $n^{xx}(\omega)$, $n^{yy}(\omega)$, and $n^{zz}(\omega)$ at static limit are listed at Table 1. Following Figure 1i we can see that at energy around 3.5 eV $[\text{Sb}_7\text{S}_8\text{Br}_2](\text{AlCl}_4)_3$ shows the highest refractive indices; then it decreases reaching its lowest value at higher energies around 13.5 eV. A remarkable finding, we note that the refractive indices of this single crystal show considerable anisotropy, which is important for SHG and OPO as it is defined by the phase-matching condition. One can obtain the phase-matching angle for the SHG (the angle between the optical beam and the optical axis for which the ω and 2ω beams are phase-matched). The birefringence can be evaluated from the linear response functions. The birefringence is defined as a difference between the extraordinary and ordinary refraction indices, $\Delta n(\omega) = n_e(\omega) - n_o(\omega)$, where $n_o(\omega)$ is the index of refraction for an electric field oriented along the c -axis (ordinary index of refraction) and $n_e(\omega)$ is the index of refraction for an electric field perpendicular to the c -axis (extraordinary index of refraction). It is clear that the birefringence is crucial only in the nonabsorbing spectral range, which is below the energy gap. The values of the birefringence at the static limit and at $\lambda = 1064$ nm were listed in Table 1.

Due to the wide optical transparency region and noncentrosymmetric structure of $[\text{Sb}_7\text{S}_8\text{Br}_2](\text{AlCl}_4)_3$, we investigated its



(a) Upper panel (b) Lower panel

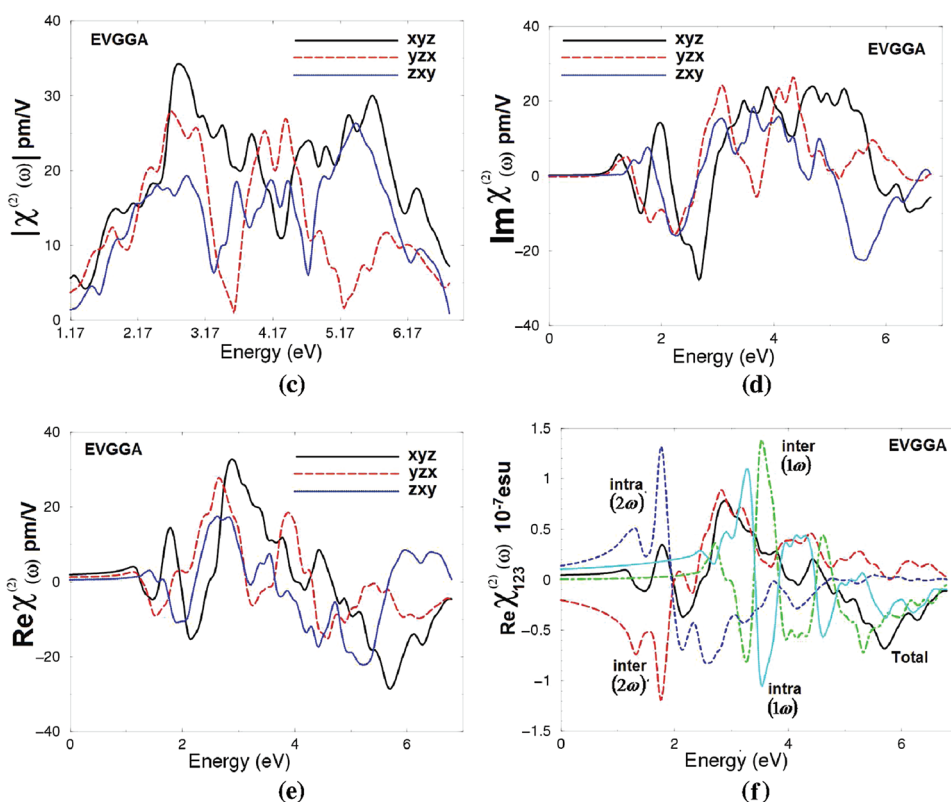


Figure 2. (a) Calculated $|\chi_{123}^{(2)}(\omega)|$ (dark solid curve, black color online), $|\chi_{231}^{(2)}(\omega)|$ (light solid curve, red color online), and $|\chi_{312}^{(2)}(\omega)|$ (light dashed curve, blue color online) using EVGGA with scissors correction. (b) Calculated $\epsilon_2^{xx}(\omega)$ (dark solid curve, black color online), $\epsilon_2^{yy}(\omega)$ (light long dashed curve, red color online), and $\epsilon_2^{zz}(\omega)$ (light dashed curve, green color online) spectra; calculated $\epsilon_2^{xx}(\omega/2)$ (dark solid curve, blue color online), $\epsilon_2^{yy}(\omega/2)$ (light long dashed curve, brown color online), and $\epsilon_2^{zz}(\omega/2)$ (light dashed curve, cyan color online) spectra. (c) Calculated $|\chi_{123}^{(2)}(\omega)|$ (dark solid curve, black color online), $|\chi_{231}^{(2)}(\omega)|$ (light solid curve, red color online), and $|\chi_{312}^{(2)}(\omega)|$ (light dashed curve, blue color online) at $\lambda = 1064$ nm using EVGGA with scissors correction. (d) Calculated $\text{Im}(\chi_{123}^{(2)}(\omega))$ (dark solid curve, black color online), $\text{Im}(\chi_{231}^{(2)}(\omega))$ (light dashed curve, red color online) spectra, and $\text{Im}(\chi_{312}^{(2)}(\omega))$ (light dashed curve, blue color online) using EVGGA with scissors correction. (e) Calculated $\text{Re}(\chi_{123}^{(2)}(\omega))$ (dark solid curve, black color online), $\text{Re}(\chi_{231}^{(2)}(\omega))$ (light dashed curve, red color online) spectra, and $\text{Re}(\chi_{312}^{(2)}(\omega))$ (light dashed curve, blue color online) using EVGGA with scissors correction. (f) Calculated total $\text{Re}(\chi_{231}^{(2)}(\omega))$ spectrum (dark solid curve, black color online) along with the intra $(2\omega)/(1\omega)$ (light dashed curve, blue color online)/ (light dashed dotted curve, yellow color online) and inter $(2\omega)/(1\omega)$ (light long dashed curve, red color online)/ (light dotted curve, green color online) band contributions. Here all $\text{Re}(\chi_{231}^{(2)}(\omega))$ are multiplied by 10^{-7} , in esu units.

Table 2. Calculated $|\chi_{ijk}^{(2)}(0)|$ and $|\chi_{ijk}^{(2)}(\omega)|$ (pm/V) at $\lambda = 1064$ nm along with d_{ijk} Values, Where $1 \text{ pm/V} = 2.387 \times 10^{-9} \text{ esu}$

tensor components	theory $\chi_{ijk}^{(2)}(0)$ (pm/V)	theory $d_{ijk} = 0.5\chi_{ijk}^{(2)}$ (0) (pm/V)	theory $\chi_{ijk}^{(2)}(\omega)$ (at $\lambda = 1064$ nm) (pm/V)	theory $d_{ijk} = 0.5\chi_{ijk}^{(2)}(\omega)$ (at $\lambda = 1064$ nm) (pm/V)
$ \chi_{123}^{(2)}(\omega) $	2.0	1.0	5.6	2.8
$ \chi_{231}^{(2)}(\omega) $	1.3	0.65	3.7	1.85
$ \chi_{312}^{(2)}(\omega) $	0.6	0.3	1.4	0.07
$\text{Re}(\text{total } \chi_{231}^{(2)}(\omega))$	0.06	0.03	0.09	0.045
$\text{Re}(\chi_{231}^{(2)}(\omega))$ (intra- (1ω))	0.11	0.055	0.15	0.075
$\text{Re}(\chi_{231}^{(2)}(\omega))$ (intra- (2ω))	0.14	0.07	0.48	0.24
$\text{Re}(\chi_{231}^{(2)}(\omega))$ (inter- (1ω))	0.01	0.005	0.01	0.005
$\text{Re}(\chi_{231}^{(2)}(\omega))$ (inter- (2ω))	−0.2	−0.1	−0.55	−0.275

NLO—SHG response. The space group $P2_12_12_1$ possesses two crystallographic symmetry elements and has several components which are equal to zero. The symmetry allows only three nonzero complex second-order nonlinear optical susceptibility tensors $\chi_{123}^{(2)}(-2\omega;\omega;\omega)$, $\chi_{231}^{(2)}(-2\omega;\omega;\omega)$, and $\chi_{312}^{(2)}(-2\omega;\omega;\omega)$. For simplicity we can write the complex second-order nonlinear optical susceptibility tensor as $\chi_{ijk}^{(2)}(\omega)$. The calculated complex second-order nonlinear optical susceptibility tensors with LDA results in incorrect complex second-order nonlinear optical susceptibility tensors since they are more sensitive to the band energy gap than the linear one due to higher power energy differences in the denominators of the complex second-order nonlinear optical susceptibility tensors formalism.^{22,23} To avoid the problem of the well-known LDA underestimation of the band gap, we have used EV-GGA for calculating the complex second-order nonlinear optical susceptibility tensors since it produces a better band gap with respect to experiment; however it is still underestimates the energy band gap by around 0.15 eV. To avoid this drawback, we consider quasi-particle self-energy corrections at the level of scissor operators in which the energy bands are rigidly shifted to merely bring the calculated energy gap closer to the experimental gap. We should emphasize that the scissor corrections have a profound effect on the magnitude of $|\chi_{ijk}^{(2)}(\omega)|$; see Figure 2a.

We can identify the origin of the spectral peaks in this figure as caused by $2\omega/\omega$ inter-/intraband contributions in the linear dielectric function. Unlike the linear optical dispersion, the features in the complex second-order nonlinear optical susceptibility tensors are more difficult to identify from the band structure because of the presence of 2ω and ω terms. But we can use the linear optical dispersion to identify the different resonances leading to various features in the complex second-order nonlinear optical susceptibilities spectra. To analyze the features of the calculated $\chi_{123}^{(2)}(\omega)$, $\chi_{231}^{(2)}(\omega)$, and $\chi_{312}^{(2)}(\omega)$ spectra, it would be helpful to compare the absolute value of the dominant component $|\chi_{123}^{(2)}(\omega)|$ (Figure 2a) with the absorptive part of the corresponding dielectric function $\varepsilon_2(\omega)$. Therefore, the calculated $\varepsilon_2(\omega)$ is shown in Figure 2b as a function of both $\omega/2$ and ω . The first structure $|\chi_{123}^{(2)}(\omega)|$ between 1.0 and 3.2 eV is mainly originated from 2ω resonance [see $\varepsilon_2(\omega/2)$, Figure 2b]. The second structure between 3.2 and 4.8 eV is associated with interference between 2ω and ω resonances (the threshold of $\varepsilon_2(\omega)$) [see $\varepsilon_2(\omega/2)$ and $\varepsilon_2(\omega)$, Figure 2b]. The last spectral structure (within 4.8–6.8 eV) is mainly due to ω resonance and is associated with the first structure in $\varepsilon_2(\omega)$. The calculated $|\chi_{ijk}^{(2)}(\omega)|$ for three tensor components are illustrated in Figure 2a. One can see that $|\chi_{123}^{(2)}(\omega)|$ is the dominant component, giving the highest value of $|\chi_{ijk}^{(2)}(\omega)|$ at both the zero frequency and at 1.165 eV ($\lambda = 1064$ nm; see Figure 2a,c).

The calculated $|\chi_{ijk}^{(2)}(0)|$ and $|\chi_{ijk}^{(2)}(\omega)|$ at $\lambda = 1064$ nm for all three tensor components are evaluated and listed in Table 2. The static values of the second-order susceptibility tensor are very important and can be used to estimate the relative SHG efficiency.

The calculated dispersions of imaginary and real parts of complex second-order nonlinear optical susceptibility tensors are shown in Figure 2d,e. Both ω and 2ω resonances can be further separated into interband and intraband contributions; see Figure 2g, which shows the real part of the dominant component along with the $2\omega/\omega$ inter-/intraband contributions. We note the opposite signs of the two contributions throughout the frequency range. It is clear that the complex second-order nonlinear optical susceptibility tensors is zero below half the band gap (i.e., < 1.01 eV) and slowly increases after half the band gap since the 2ω resonance begins to contribute at energies above half the band gap (i.e., > 1.0 eV) due to $E-2\omega$ terms in the denominator of the formalism of the complex second-order nonlinear optical susceptibility tensors.^{22,23} The ω resonance begins to contribute for energy values above the energy gap. At low spectral range (below half the energy band gap) the SHG optical spectra are dominated by the 2ω contributions. Beyond the fundamental energy gap (i.e., > 2.03 eV) the major contribution comes from the ω term.

From the calculated $\chi_{ijk}^{(2)}(\omega)$ dispersion we have obtained the microscopic second-order hyperpolarizability, β_{ijk} , the vector components along the dipole moment direction. The microscopic second-order hyperpolarizability terms cumulatively yield a bulk observable second-order susceptibility term, $\chi_{ijk}^{(2)}(\omega)$, which in turn is responsible for the high SHG response.^{24,25} For the dominant component $|\chi_{123}^{(2)}(\omega)|$ we have calculated β_{123} at the static limit and at $\lambda = 1064$ nm, using the expression given in ref 23. We have found that these values are equal to 8.012×10^{-30} esu at static limit and 22.43×10^{-30} esu at $\lambda = 1064$ nm. To justify its possible application as nonlinear optical material, we can compare this value with the calculated and measured value (31.6×10^{-30} esu at $\lambda = 1064$ nm) of the dominant component $|\chi_{333}^{(2)}(\omega)|$ of the potassium titanyl phosphate KTiOPO_4 (KTP),²⁶ the well-known nonlinear optical single crystal that is commonly used for frequency doubling diode pumped solid-state lasers, such as Nd:YAG, and other neodymium-doped lasers. We believe that this work opens up a novel possibility to interpret the obtained optical functions of organic and inorganic materials and to know the partial contributions of molecular groups.

V. CONCLUSIONS

We have presented calculations of the dispersion of linear and nonlinear optical susceptibilities in an ionic liquid single crystal

for the relaxed geometry using density functional theory. We find the fundamental optical absorption edge is located at 2.0 eV in excellent agreement with the experimental data. We show the results of calculations for $\epsilon_2^{xx}(\omega)$, $\epsilon_2^{yy}(\omega)$, and $\epsilon_2^{zz}(\omega)$. This compound possesses a considerable anisotropy in the linear optical susceptibilities which favors enhanced phase matching conditions necessary for the observation of SHG and OPO. Our calculations show that in $[\text{Sb}_7\text{S}_8\text{Br}_2](\text{AlCl}_4)_3$, $|\chi_{123}^{(2)}(\omega)|$ is dominant SHG component which gives the highest value of $|\chi_{ijk}^{(2)}(\omega)|$ at both the zero frequency and at 1.165 eV ($\lambda = 1064$ nm). The microscopic second-order hyperpolarizability of the dominant SHG component, β_{123} , was calculated at the static limit and at $\lambda = 1064$ nm.

AUTHOR INFORMATION

Corresponding Author

*Tel.: +420 777729583. Fax: +420-386 361231. E-mail address: maalidph@yahoo.co.uk.

ACKNOWLEDGMENT

This work was supported from the institutional research concept of the Institute of Physical Biology, UFB (Grant No. MSM6007665808), the program RDI of the Czech Republic, the project CENAKVA (Grant No. CZ.1.05/2.1.00/01.0024), Grant No. 152/2010/Z of the Grant Agency of the University of South Bohemia, and the School of Material Engineering, Malaysia University of Perlis, Malaysia.

REFERENCES

- (1) Audrieth, L. F.; Long, A.; Edwards, R. E. *J. Am. Chem. Soc.* **1936**, *58*, 428–429.
- (2) MacFarlane, D. R.; Golding, J.; Forsyth, S.; Forsyth, M.; Deacon, G. B. *Chem. Commun. (Cambridge, U. K.)* **2001**, 1430–1431.
- (3) Crosthwaite, J. M.; Muldoon, M. J.; Dixon, J. K.; Anderson, J. L.; Brennecke, J. F. *J. Chem. Thermodyn.* **2005**, *37*, 559–568.
- (4) http://www.google.com/patents/about?id=4K_IAAAAE-BAJ&dq=7588694, mixture of nitrate salts with mp below 100 °C.
- (5) Barrer, R. M. *Trans. Faraday Soc.* **1943**, *39*, 59–67.
- (6) Morris, R. E. *Angew. Chem., Int. Ed.* **2008**, *47*, 442–444.
- (7) (a) Migowski, P.; Dupont, J. *Chem. Eur. J.* **2007**, *13*, 32–39. (b) Guloy, A. M.; Ramlau, R.; Tang, Z.; Schnelle, W.; Baitinger, M.; Grin, Y. *Nature* **2006**, *443*, 320–323.
- (8) (a) Aumann, M.; Riisager, A. *Chem. Rev.* **2008**, *108*, 1474–1497. (b) Tundo, P.; Perosa, A. *Chem. Soc. Rev.* **2007**, *36*, 532–550.
- (9) Han, X.; Armstrong, D. W. *Acc. Chem. Res.* **2007**, *40*, 1079–1086.
- (10) El Abedin, S. Z.; Endres, F. *Acc. Chem. Res.* **2007**, *40*, 1106–1113.
- (11) Lodge, T. P. *Science* **2008**, *321*, 50–51.
- (12) Hsu, K. F.; Loo, S.; Guo, F.; Chen, W.; Dyck, J. S.; Uher, C.; Hogan, T.; Polychroniadis, E. K.; Kanatzidis, M. G. *Science* **2004**, *303*, 818–821.
- (13) Zhang, Q.; Chung, I.; Jang, J. I.; Ketterson, J. B.; Kanatzidis, M. G. *J. Am. Chem. Soc.* **2009**, *131*, 9896–9897.
- (14) Reshak, A. H.; Kamarudin, H.; Auluck, S.; Minofar, B.; Kityk, I. V. *Appl. Phys. Lett.* **2011**, *98*, No. 201903.
- (15) Harrison, W. T. A.; Phillips, M. L. F.; Stucky, G. D. *Chem. Mater.* **1995**, *7*, 1849–1856.
- (16) Hohenberg, P.; Kohn, W. *Phys. Rev. B* **1964**, *136*, 864–871.
- (17) Blaha, P.; Schwarz, K.; Madsen, G. K. H.; Kvasnicka, D.; Luitz, J. *WIEN2K*, “an augmented plane wave + local orbitals program for calculating crystal properties”; Karlheinz Schwarz, Technische Universität Wien, Austria, 2001; ISBN 3-9501031-1-2.
- (18) Ceperley, D. M.; Ader, B. I. *Phys. Rev. Lett.* **1980**, *45*, 566–569.
- (19) Engel, E.; Vosko, S. H. *Phys. Rev. B* **1993**, *47*, 13164–13174.
- (20) Tributsch, H. Z. *Naturforsch., A: Phys. Sci.* **1977**, *32*, 972–985.
- (21) Wooten, F. *Optical Properties of Solids*; Academic Press: New York, 1972.
- (22) (a) Rashkeev, S. N.; Lambrecht, W. R. L. *Phys. Rev. B* **2001**, *63*, 165212–165224. (b) Rashkeev, S. N.; Lambrecht, W. R. L.; Segall, B. *Phys. Rev. B* **1998**, *57*, 3905–3919.
- (23) Reshak, A. H. Ph.D. thesis, Indian Institute of Technology—Roorkee, India, 2005.
- (24) Boyd, R. W. *Principles of Nonlinear Optics*; Academic Press: New York, 1982; p 420.
- (25) Boyd, R. W. *Nonlinear Optics*, 3rd ed.; Academic Press: New York, 2008; ISBN 978-0-12-369470-6.
- (26) Reshak, A. H.; Kityk, I. V.; Auluck, S. J. *Phys. Chem. B* **2010**, *114*, 16705–16712.